The DOI for this manuscript is doi: 10.1175/JCLI-D-16-0396.1

The final published version of this manuscript will replace the preliminary version at the above DOI once it is available.

If you would like to cite this EOR in a separate work, please use the following full citation:

Desbruyères, D., E. McDonagh, B. King, and V. Thierry, 2016: Global and Full-depth Ocean Temperature Trends during the early 21st century from Argo and Repeat Hydrography. J. Climate. doi:10.1175/JCLI-D-16-0396.1, in press.

Global and Full-depth Ocean Temperature Trends during the early 21st century from Argo and Repeat Hydrography

Damien Desbruyères*, Elaine L. McDonagh, Brian A. King

National Oceanography Centre, Southampton, UK

Virginie Thierry

IFREMER, Brest, France

**Corresponding author address:* Damien Desbruyères, National Oceanography Centre, European Way, SO14 3ZH, Southampton, UK.

E-mail: dades@noc.ac.uk

ABSTRACT

The early 21st century's warming trend of the full-depth global ocean is calculated by combining the analysis of Argo (top 2000m) and repeat hydrography into a blended full-depth observing system. The surface-to-bottom temperature change over the last decade of sustained observation is equivalent to a heat uptake of 0.72 ± 0.09 W m^{-2} applied over the surface of the earth, 90% of it being found above 2000m depth. We decompose the temperature trend point-wise into changes in isopycnal depth (heave) and temperature changes along an isopycnal (spiciness) to describe the mechanisms controlling the variability. The heave component dominates the global heat content increase, with the largest trends found in the southern hemisphere's extratropics (0 - 2000m) highlighting a volumetric increase of subtropical mode waters. Significant heave-related warming is also found in the deep North Atlantic and Southern Ocean (2000m - 4000m), reflecting a potential decrease in deep water mass renewal rates. The spiciness component shows its strongest contribution at intermediate levels (700m - 2000m), with striking localised warming signals in regions of intense vertical mixing (North Atlantic and Southern oceans). Finally, the agreement between the independent Argo and repeat hydrography temperature changes at 2000m provides an overall good confidence in the blended heat content evaluation on global and ocean scales, but also highlights basin scale discrepancies between the two independent estimates. Those mismatches are largest in those basins with the largest heave signature (Southern Ocean) and reflect both the temporal and spatial sparseness of the hydrography sampling.

1. Introduction

Since the mid-20th century, the Earth's climate system has undergone human-induced changes with potentially large socio-economical impacts. Those changes include increasing global oceanic heat content (OHC) representing about 93% of the Earth's heat uptake (Intergovernmental Panel on Climate Change 2013). Major international and national efforts are underway to monitor this key climatic variable and understand the physical basis behind its variability, as a prerequisite for better regional and global predictions. These efforts rely on the development of sustained global observational networks from shipboard and autonomous systems. While the first survey of the full-depth coast-to-coast oceans by the World Ocean Climate Experiment (WOCE) shed new light on the physical properties (temperature, salinity, velocity) of the global ocean interior (e.g. Ganachaud and Wunsch 2003), the follow-up surveys supported by the Climate Variability, Predictability and Change (CLIVAR) and the Global Ocean Ship-based Hydrographic Investigations (GO-SHIP) programs enabled quantification of changing properties including global oceanic warming (e.g. Purkey and Johnson 2010). For the most recent decade, the decadal repeat of hydrographic sections is being supplemented by the Argo array, which reached its target fleet size in 2007 with 3000 floats sampling the top two kilometres of the water column on a nominal 10-day cycle (Roemmich and Gilson 2009). The Argo program has revolutionised our understanding of properties, circulation, and associated climate variability in the upper 2000m of the ocean.

Using the unprecedented sampling resolution of the Argo array, many of the recent analyses of OHC variability described the upper half of the water column. Estimates of the globally-averaged warming trends above 2000m fall within the range 0.3 to 0.7 W m^{-2} during the years 2006-2012 (von Schuckmann et al. 2016). The most recent estimate is between 0.5 to 0.65 W m^{-2} over the Argo-sampled regions during 2006-2015 (Wijffels et al. 2016). While the observational record is becoming complete enough to ascertain the ongoing rise of the Earth's energy content, the slowdown of global surface temperature rise - or *hiatus* - during the 2000's (Trenberth and Fasullo 2010) has increased interest in analysis of the regional and vertical signatures of that global trend (e.g. Meehl et al. 2011; England et al. 2014; Kostov et al. 2014; Drijtfhout et al. 2014; Chen and Tung 2014). Model studies have particularly emphasised the need to measure temperature changes throughout the whole water column to average out vertical rearrangements and hence capture the anthropogenic warming more effectively (e.g. Palmer et al. 2015).

Focusing on the 1990's to 2000's trend, Purkey and Johnson (2010) reported the significance of the deep and abyssal layers in the global heat budget, with a hydrography-derived warming rate below 2000 m depth representing about 10-15% of the current trend captured by Argo above 2000m. Continuing international efforts coordinated by GO-SHIP have now produced another decade of repeat hydrography sections around the globe. These sections allow some first quantifications of deep and abyssal ocean changes during the most recent decade, complementing the results obtained via Argo. We therefore extend the regional analysis of Desbruyères et al. (2014) to the near-global ocean, using a blend of Argo and shipboard repeat hydrography data for the analysis of OHC trends throughout the water column. In addition to providing estimations of the full-depth OHC changes on global and regional scale during the last decade of sustained observations, the blended Argo-Hydrography estimates will be used to characterise some limitations of the current deep observing system.

Argo-based OHC trend estimates show strong regional variations (e.g. Roemmich et al. 2015) reflecting the dynamical redistribution of heat laterally and vertically on time scales ranging from weeks to decades. Understanding the anthropogenic imprint on the ocean will be informed by diagnosing the mechanisms and controls of regional temperature changes. Here, we follow Bindoff and McDougall (1994) and use a decomposition of the temperature variability into changes in water mass property along isopycnals (referred to as spiciness herein) versus changes related to vertical displacements of isopycnals (referred to as 'heave herein). Spiciness represents a shift of the θ/S profiles, which implies density-compensated changes in θ and S. The passive spreading of spice anomalies by the general circulation and their resurfacing at a remote location is one of the key mechanisms for climate variability teleconnections (Johnson et al. 2005). Heave represents the change in temperature at a fixed depth due to either adiabatic (e.g. wind forcing) or diabatic (e.g. subduction of warm waters) processes that leads to vertical migrations of isopycnal surfaces. This heave/spiciness decomposition, which was first proposed by Bindoff and McDougall (1994), has been recently used to characterize the historical patterns of the global OHC in the upper 700m of the water column from ocean reanalysis products and ocean state estimates (Häkkinen et al. 2016). The authors highlighted that the multi-decadal warming climate was accompanied by a remarkable deepening of mid-thermocline isopycnals, reflecting the lateral spreading of heat from high-latitude ventilation regions and a global expansion of subtropical mode waters (e.g. Church et al. 1991). Deeper in the water column, heave-related temperature changes on decadal scale were also reported around Antarctica in the depth range of Antarctic Bottom Water (Purkey and Jonhson 2012) and in the North Atlantic Subpolar Gyre in the depth range of Labrador Sea Water (Desbruyères et al. 2014), suggesting transport changes associated with the lower limb of the meridional overturning circulation. The heave/spiciness decomposition, which has not yet been assessed from full-depth global measurements, is here applied to the blended Argo-Hydrography estimate to complement the description of the regional and vertical distribution of OHC during the early 21^{st} century.

The paper is structured as follows. Section 2 describes the Argo and hydrography datasets used herein. Section 3 describes the three-dimensional distribution of temperature trend and associated OHC. Section 4 focuses on the respective contribution of heave and spiciness variability, and

Section 5 discusses the degree of agreement between the independent estimates provided by Argo and repeat hydrography. Section 6 discusses and summarises the main results.

2. Data and methods

The spatial and temporal distributions of the Argo and hydrography datasets are shown in Figure 1. For their analysis, 33 basins defined by bathymetry and climatological bottom temperature (Purkey and Johnson 2010) will be assembled into four groups: Atlantic (red), Pacific (dark blue), Indian (green) and Southern (light blue). Following common practice, the description of the vertical patterns will refer to the 0-700m, 700m-2000m, 2000m-4000m and 4000m-6000m layers as the upper, intermediate, deep and abyssal layers, respectively.

a. Argo

The upper and intermediate layers of the water column are analysed using Argo profiles gathered every 10 days between January 2006 and December 2014 and passed through Argo Delayed Mode Quality Control (http://doi.org/10.17882/42182). This time period was chosen following the thorough error analysis of Roemmich et al. (2015) that showed the inadequacy of the Argo array prior to 2006 when studying global ocean trends. The accuracy of temperature, salinity and pressure measurements are 0.002°C, 0.01 psu and 2.4 dbar, respectively (Roemmich and Gilson 2009). Optimal interpolation (OI) is used to select and map Argo profiles on a regular 2° grid with a 20 db vertical resolution, as described in Desbruyères et al. (2014) and detailed below. Regions of highest float densities are found in the northeastern Atlantic, the south Australian basin, the subtropical Pacific and the Kuroshio area (Figure 1b). Fewer measurements are available in the subtropical South Atlantic and along continental boundaries (especially Antarctica). The Arctic

Ocean and the Caribbean, Mediterranean and Indonesian Seas are not included in the present study due to lack of data.

The OI was carried out on density surfaces (rather than depth surfaces for instance) in order to preserve the water mass temperature/salinity structure, and temperature anomalies were referenced to a 2005-2012 climatological field that was largely based on Argo data (World Ocean Atlas 2013). For a given grid point, the OI determines the weights to be assigned to the surrounded Argo profiles according to the spatial distribution and the spatial covariance of those profiles. The weights, determined with a spatial length scale of 500 km, provide the optimal estimate of the mean anomaly to be mapped. If the data surrounding the grid point is sparse, the mapping error returned by the OI will be consequently high.

The year-long continuous time-series of temperature obtained from the OI were smoothed point-wise with a 12-month running mean for removing the seasonal cycle (note that subtracting the monthly average from each corresponding months yields similar results). The temperature tendency with time at each grid point was obtained via a linear regression (in the least-square sense) and the associated standard error of the local temperature tendency (SSE) at each grid point was derived by combining the time series of the formal mapping error ε from the OI and the time series of the residual misfit of the trend r (assuming independency of ε and r) as:

$$SSE = \sqrt{\frac{\sum(r^2+\varepsilon^2)}{(n-2)\sum(x-\bar{x})^2}} \tag{1}$$

where n is the number of observations, and x is time. The number of degree of freedom (DOF) of each time series was computed by dividing the length of the time series by its autocorrelation timescales (i.e. first zero crossing of the autocorrelation sequence). The numbers of DOF show small spatial variability within the global domain, with values of about 10 ± 3. We choose 10 DOF as a typical value for converting the SSE into a 95% confidence interval, following Student t-test distribution. The gridded fields of temperature trends are finally averaged over ocean basins to examine the vertical structure of the temperature trend (e.g. Figure 2). This is done using the fractional area of individual grid points as a weight in the integration. Similarly, averaged errors are computed as the arithmetic weighted sum of the error, providing the upper (conservative) bounds of the uncertainties at each pressure level (e.g Levitus et al. 2012). Trend estimates and their errors are also averaged over depth intervals to examine the regional distribution of the temperature trend (e.g. Figure 3).

b. Repeat hydrography

The deep and abyssal layers of the water column are analysed using shipboard conductivity-temperature-depth (CTD) data from 60 hydrography repeats carried out along 18 sections since the year 2000 (Figure 1a and Figure 1c). The North Atlantic has the densest sampling, whilst the northern Indian, the eastern tropical Pacific and some parts of the Southern Ocean remain unsampled. The current standards for such measurements are 0.002°C for temperature, 0.002 psu for salinity and 3 dbar for pressure (Hood et al. 2010). The underlying methodology has been described previously in Purkey and Johnson (2010) and Desbruyères et al. (2014). For each section, the temperature fields are interpolated along a nominal cruise track on a 3 kilometres x 20 db grid and the linear trend at every grid point is computed from the available number of repeats. We calculate a mean temperature trend and its standard deviation at every pressure level for each of the 23 basins sampled by repeat hydrography by dividing the sections at the basin boundaries. We note here that the repeat hydrography reference sections are designed with the aim of having one repeat section in each basin, with this section being representative of that ocean basin. If a basin is crossed by more than one section, the length-weighted average and standard deviation are used. The uncertainty of the mean trend at every pressure level for each basin is computed by dividing the mean standard deviation of the trend by the square root of a number of degree of freedom. The latter is derived by dividing the cumulated length of the sections crossing that basin by a horizontal decorrelation scale of 163 km (Purkey and Johnson 2010). The 95% confidence interval of the trend at every pressure level is obtained assuming a Student t-test distribution. We note here that such uncertainty represents a commission error. Omission error will be evaluated independently in Section 5 by combining hydrography and Argo-derived trends at the 2000 db horizon. The area of each basin at each pressure level is finally used as a weight to compute five distinct averaged profiles for the Atlantic, Pacific, Indian, Southern and Global oceans (e.g. Figure 2).

Altogether, the sections describe the mean time span 2003-2012, obtained by averaging the dates of the first and last occupations of all sections. However, the temporal inhomogeneity of the hydrography sampling implies that the time-spans described may slightly differ between sections and hence from one basin to the other. The underlying methodology (Purkey and Johnson 2010) hence assumes that the linear temperature trends computed along each section are representative of a common time-span. Moreover, such timing restrictions of the hydrography sampling means that it cannot precisely match the chosen Argo window (January 2006 - December 2014), introducing potential temporal biases when merging the two independent estimates. From the analysis of Roemmich et al. (2015) and Durack et al. (2014), we argue that stronger OHC biases would be introduced above 2000m if the early years of Argo (2003-2005) were included to better match the hydrography window. The agreement between the two independent datasets will be further detailed and discussed in Section 5.

3. The spatial distribution of temperature changes

The ocean temperature change is presented in two ways. The first is the average temperature change in m°C yr^{-1} at each pressure level (lines in Figure 2). The second is the OHC trend in W m^{-2} within each 100 m bin (bars in Figure 2, with unit of 10^{-3} W m^{-2} for clarity), computed by multiplying the average temperature trend of individual 100 m layer by the volume, the density and the thermal heat capacity of the layer. The structures of the average temperature trend and the associated average OHC trends differ as the latter also depends on the volume of the 100m-thick layers. Note that the average OHC trends are presented as applied over the entire surface of the Earth, in order to be directly comparable to top-of-atmosphere measurements without reference to regional or global ocean areas.

a. The global picture

The global ocean is warming at all pressure levels (Figure 2a), with warming maxima visible at the surface, 1000m, and 4200m. The full-depth average warming is 2.2 $\pm$ 0.3 m°C yr^{-1}, which corresponds to a global heat uptake of 0.72 $\pm$ 0.09 W m^{-2} (relative to the Earth surface area) and a thermosteric sea-level rise of 0.87 $\pm$ 0.13 mm yr^{-1}. All four major oceans have warmed. The Southern Ocean shows the strongest OHC trend (0.24 W m^{-2}, that is 34% of the global OHC change), followed by the Indian Ocean (0.17 W m^{-2}), the Atlantic Ocean (0.16 W m^{-2}), and the Pacific Ocean (0.15 W m^{-2}). The global warming rate of the 0-2000m layer (0.65 W m^{-2}) estimated from Argo explains 90% of the full-depth estimate, the remainder (0.07 W m^{-2}) is estimated by repeat hydrography in the deeper layers. Below, we focus on the temperature trends and their associated OHC trends within the four distinct layers, describing both their vertical structures (Figure 2) and their horizontal distributions (Figure 3). Figure 4 highlights the local statistical significance of the Argo-derived OHC trends and the percentage of variance they explain.

b. The upper layer

The upper 700m of the water column warms at 5 m°C yr^{-1} and accounts for 44% of the global, full-depth OHC trend. Vertical temperature change profiles highlight the similar structure of the Indian (Figure 2d) and Pacific oceans (Figure 2c), with a warming limited to the upper 500m. The Indian Ocean however shows stronger and significant trends that explain almost half of the whole upper ocean warming. The Southern Ocean (Figure 2e) depicts a cooling trend in the top 100m but a significant warming over the remaining part of the upper layer. The Atlantic Ocean (Figure 2b) presents the smallest OHC trend within the upper layer as cooling above 300m compensates for a warming below.

A detailed picture of the global 0-700m OHC trend distribution (Figure 3a,b) primarily locates the upper warming within a large extratropical band of the southern hemisphere between 20°S and 60°S encompassing the Atlantic, Pacific and Indian oceans This warming trend is statistically significant at the 95% confidence level and can locally explain more than 60% of the total variance (e.g. central Pacific; Figure 4a). Strong statistically-significant warming also occurred in the tropical Indian Ocean north of 20°S, in the northern Pacific, and in the Weddell-Enderby basin of the Southern Ocean (we note here that caution should be taken when interpreting trend values near the Antarctic continent due to potentially poor data coverage during austral winter. Although the formal mapping error (ε in equation 1) intrinsically includes such information, uncertainties may still be under-estimated by the isotropic 500 km correlation scale that might projects Antarctic Circumpolar Current's floats into southern marginal seas.) Cooling dominates in the Atlantic north of 20°S, with particularly strong trends found over the central and eastern subpolar gyre, which locally explain up to 50% of the total variance. Minor cooling trends (compared to interannual variability) are observed in the southwestern Indian Ocean, and within most of the northern subtropics (10°N and 30°N) and eastern basins of the Pacific Ocean.

c. The intermediate layer

The intermediate layer (between 700m and 2000m depth) shows an averaged warming of 3 m°C yr^{-1} and accounts by itself for 0.34 W m^{-2}, almost half of the full-depth OHC trend (Figure 2a). Ocean basin horizontal-average trends are all positive and show relatively similar structures from one ocean to the next, with warming generally diminishing with depth. The strongest averaged temperature trends are located in the Southern Ocean (Figure 2e) followed by the Atlantic Ocean (Figure 2b). Smaller averaged trends are found in the Indian and Pacific oceans (Figure 2c and 2d), although the latter's contribution to the global OHC trend remains as significant as the Atlantic Ocean and Southern Ocean due to its large volume.

The horizontal distribution of the intermediate OHC trend (Figure 3c,d) and associated uncertainties (Figure 4b) shows only a few areas with statistically-significant cooling trends (e.g. the Amundsen-Bellingshausen basin in the Pacific sector of the Southern Ocean). The overall picture is widespread warming within most of the layer, with the dominant warming feature of the upper layer found in the southern hemisphere extra tropics still visible between 700m and 2000m. In addition, two localised ”hot spots” stand out as having particularly strong and statistically significant warming in the intermediate layer: the Weddell-Enderby basin in the Southern Ocean (Atlantic sector) and the subpolar North Atlantic, with the latter explaining more than 70% of the total variance in that region.

d. The deep layer

The deep layer (2000m - 4000m) warmed globally at 0.3 m°C yr^{-1} and accounts for 7% of the full-depth OHC trend (Figure 2a). In the Southern Ocean, the vertical uniformity and the strong magnitude of the deep temperature trends are remarkable (Figure 2e), and as a result clearly dominate the global OHC trend between 2000m and 4000m. The deep warming of the Southern Ocean is observed all around Antarctica but is particularly strong in the Amundsen-Bellingshausen (Pacific sector) and Weddell-Enderby (Atlantic sector) basins (Figure 3e,f). The relatively small OHC change in the deep Atlantic (0.02 W m^{-2}) represents a compensation between a 2000m-3000m warming north of the equator and a 3000m-4000m cooling south of it. The deep Pacific Ocean shows an overall cooling trend with largest magnitude found within its westernmost basin, while variable positive and negative trends within the Indian Ocean's basins lead to a small and largely uncertain spatial average.

e. The abyssal layer

The global temperature trend in the abyssal layer (4000m - 6000m) shows a stronger magnitude than the deep trend (0.4 m°C yr^{-1}), but represents a minor contribution to the OHC trend (4%) due to a reduced ocean volume (Figure 2a). Average warming is observed in the four main oceans, although the spatial distribution of the trend shows a clear domination of the southern hemisphere's basins. We note that this pattern (Figure 3g,h) closely matches that reported in Purkey and Johnson (2010) for the preceding decades. Cooling trends are observed in the westernmost Pacific Ocean, in the Agulhas area of the Indian Ocean, and in the abyssal North Atlantic Ocean.

4. Heave versus spiciness variability

An observed temperature change at a given depth can be due to either vertical migration of isopycnal surfaces (referred to as heave, herein) and/or temperature changes along isopycnal surfaces (referred to as spiciness, herein). Following the study of Bindoff and McDougall (1994), these two contributions to the total temperature changes are here computed at every point of the Argo grid and at every grid point of the hydrography section grids, following equation 2:

$$\left.\frac{d\theta}{dt}\right|_p \approx \left.\frac{d\theta}{dt}\right|_n - \left.\frac{dp}{dt}\right|_n \left(\frac{\partial \theta}{\partial p}\right) \tag{2}$$

where $\Big|_p$ denotes changes along pressure surfaces and $\Big|_n$ denotes changes along isopycnal surfaces. Note that this decomposition was recently applied to multi-decadal reanalysis OHC products by Häkkinen et al. (2016). A residual is obtained from the difference between the true trend (left-hand side of equation 2) and the sum of both contributions (right-hand side of equation 2). Such residual is negligible over the whole water column except in the near-surface layer where the heave/spiciness decomposition is complicated by air-sea interactions and large vertical temperature gradients.

The present representation of heave (second term on the right-hand side of equation 2) does not necessarily only reflect dynamically-induced adiabatic processes, (e.g. wind-driven Ekman pumping, low frequency Rossby waves) but may also arise, for instance, through downward diffusion of the surface heating or changes in the rate of water mass renewal in subduction areas (Häkkinen et al. 2015, 2016). The spiciness component of the temperature trend represents a shift in the θ/S profiles at constant density and therefore implicitly involves a change in salinity. Here, the focus is made on the description of the vertical (Figure 5 and Figure 6) and horizontal (Figure 7) distribution of both contributions to the full-depth temperature and OHC trends of the blended Argo-hydrography estimates described in Section 3.

a. The global picture

The global and basin averaged profiles shows that the relative contribution of heave and spiciness to the total temperature and OHC trends varies both amongst oceans and layers (Figure 6). On the global scale, 63% of the full-depth OHC trend is associated with heave (Figure 6a), although this number primarily reflects a striking opposition between a heave-related warming and a spiciness-related cooling in the upper Pacific Ocean (Figure 6c). We quantify the deepening of isopycnal $\left.\frac{dp}{dt}\right|_n$ as an intermediary step in calculating the heave component of the temperature change (Figure 5). A global deepening of isopycnal surfaces is consistently seen, with the largest displacements occurring in the Atlantic and Southern oceans at the ~ 27.1 kg m^{-3} density level. In these two regions, water masses lighter than ~ 27.1 kg m^{-3} (typically subtropical mode waters) have increased their volume, while denser water masses (typically subpolar mode waters) have undergone volume loss. Such a strong deepening of mid-thermocline isopycnals was also reported from the analysis of multidecadal reanalysis products, and was interpreted as the subduction and lateral spreading of anomalous heat from the ventilation areas of subtropical mode water (Häkkinen et al. 2016). The changes in isopycnal depth in the Indian Ocean differs from that observed in the three other oceans: light isopycnals went down while heavy isopycnals went up in the water column. This potentially reflects an increased heat transport from the Pacific Ocean in the upper layer (Lee et al. 2015), and local overturning shifts with deep waters returning farther up in the water column in the late 2000s than in the early 2000s (Hernàndez-Guerra and Talley 2016). In following subsections, we focus on the horizontal distributions of the heave and spiciness temperature trends and their associated OHC trends within the four distinct layers.

b. The upper layer

As stated above, the description of heave and spiciness within the uppermost layer is hampered by strong residuals near the surface (see dashed lines in Figure 6) and we therefore only evaluate the changes between 200m and 700m. The predominance of heave on the global OHC increase above 700m still stands out (Figure 6a), with the strongest averaged contributions to the global OHC found in the Indian and Pacific oceans (Figure 6c and Figure 6d). In both the Atlantic and Southern Ocean, the averaged heave trends mostly compensate within the upper layer (cooling above 400m and warming below), leaving spiciness as the dominant contributor to the OHC increase (Figure 6b and 6e).

The detailed horizontal distribution of heave and spiciness within the upper layer shows the largest heave-induced warming within the southern hemisphere extra-tropical band between 20°S and 60°S and in the subtropical North Pacific (Figure 7a). These heave-related warming trends are significantly damped by cooling along isopycnal revealed by the spiciness component of the trend (Figure 7b). This opposition between the two components of the total trend is consistent with the ”pure warming” scenario of a typical subtropical water column (warm/salty waters over cold/fresh waters) described by Bindoff and McDougall (1994), where the subsurface warming separates into positive heave and negative spiciness. The opposite situation is usually found in subpolar regions (warm/fresh waters over cold/salty waters) where both components tend to have the same sign. This is here verified in the subpolar North Atlantic (heave and spice cooling), and with a smaller magnitude in the Atlantic sector of the Southern Ocean (heave and spice warming).

c. The intermediate layer

Both heave and spiciness are significantly involved in warming the global 700m-2000m intermediate layer and explain 40% and 60% of the global OHC trend, respectively (Figure 6a). In the

Indian Ocean, isopycnal surfaces within the intermediate depth range were found to move upward in the water column (26.9 - 27.3 kg m^{-3} density range in Figure 5), and the averaged heave trend is consistently negative in that basin (Figure 6d). The averaged heave trends are positive in the three other oceans, with only few areas showing heave-related cooling: the western Pacific, the eastern Indian, the Amundsen-Bellingshausen basin in the Southern Ocean (Pacific sector) and the equatorial North Atlantic (Figure 7d). The heave-related warming trends of the northwestern Pacific and of the southern hemisphere extra tropics that were found to dominate the upper layer picture are deep-reaching signals, still visible in the intermediate layer. Heaving also causes a warming of the Atlantic Ocean north of 20°N, which is further augmented by isopycnal warming in the subpolar gyre (north of 40°N) and diminished by isopycnal cooling in the western subtropical area between 20°N and 40°N (Figure 7e). Nonetheless, the most striking signal within the intermediate layer is a strong increase of temperature along isopycnal in the Weddell-Enderby basin of the Southern Ocean (Atlantic sector), explaining by itself almost half of the global spiciness OHC trend within that layer.

d. The deep and abyssal layers

The global 2000m-4000m deep layer shows a heave-related warming (Figure 6a), which is primarily found in the Atlantic and Southern oceans (Figure 7g). Strong heave-related cooling trends are found in the westernmost Pacific Ocean and within most of the Indian Ocean. The spiciness trend is negative within most of the deep layer, except in the northwestern Atlantic and Southern Ocean basins (Figure 7h). Finally, the OHC trend associated with the abyssal warming is, on the global scale, mostly induced by heave (Figure 6a) although the temperature trends associated with spiciness become increasingly important near the ocean bottom within the four major oceans (Figure 6b,c,d,e), with the strongest signals found in the southern hemisphere (Figure 7j).

5. The agreement between Argo and repeat hydrography at 2000m

Temperature trends deeper than 2000m (Sections 3d and 3e) are calculated from the analysis of relatively sparse repeat hydrographic sections (Figure 1). The uncertainty that we report for these hydrography-derived trends is a standard error and relates to how well the mean of the trend is described by the sections in a basin, or ocean or globally. Essentially this uncertainty reflects how spatially comprehensive sampling on repeat hydrographic section is. Here, we investigate further the nature of the hydrography-derived uncertainty by considering the mismatch between the hydrography-based trends at 2000m and the independent Argo-based values at 2000m, allowing us to assess an additional source of uncertainty associated with the deep observing system.

Overall, the globally averaged temperature trend reveals a good agreement between the independent Argo-based values at 2000m and the corresponding hydrography values, such that the Argo estimate agrees (to within uncertainty) with the repeat hydrography temperature change at that depth (Figure 2a). Although this overall agreement gives good confidence in the blended estimates of the OHC trend, the extent to which the two independent datasets agree with each other varies between basins. Those mismatches can be partly attributed to the slightly different time-windows described by both datasets, but we argue that they primarily arise from high frequency signals (monthly to interannual) that alias the relatively sparse hydrography sampling. This hypothesis is supported by larger discrepancies between the observing systems associated with the heave component of the trend (Figure 6), which is more likely to be influenced by high-frequency ocean dynamics and fast adiabatic redistributions not easily resolved by the synoptic hydrography repeats. Furthermore, the largest mismatches between Argo and hydrography are found in the Atlantic and Southern oceans (Figure 2b and 2e), which is consistent with the relatively deep extension of intense dynamical regimes associated with deep-water formation processes and MOC-type cells.

We interpret the mismatch between the Argo and hydrography-derived trends at 2000m as representing the combined impact of spatial and temporal sparseness of the hydrography repeats (referred to as the total mismatch hereafter). In Figure 8a we show the total mismatch versus the hydrography uncertainty. In the majority of basins the total mismatch is larger than the hydrography uncertainty (points lie to the right of the red 1:1 line, Figure 8a), implying that on average the hydrography uncertainty is an underestimate of the total uncertainty. Basins with the largest total mismatch are in the Southern Ocean. In the Atlantic and Indian Oceans more basins have total mismatch (uncertainty) greater than the hydrography uncertainty than less than it. However in the Pacific all except one basin lies to the left of the 1:1 line and the hydrography uncertainty is a not an underestimate of the total uncertainty.

We further analyse the total mismatch at 2000m into a spatial and temporal contribution by subsampling the Argo data along the hydrographic sections. We compare the temperature trends from the subsampled Argo data with the full Argo data and refer to the difference as the spatial mismatch (Figure 8b). We then compare the temperature trends from the subsampled Argo data with the temperature trends at 2000m from hydrographic data and refer to the difference as the temporal mismatch (Figure 8c). The majority of basins show spatial mismatch smaller than the hydrography-derived uncertainties (to the left of the red 1:1 line in Figure 8b), and temporal mismatches larger than the hydrography-derived uncertainties. Thus analysis further supports our hypothesis that the hydrography-derived uncertainties (e.g. Figure 2) are a good measure of the spatial representativeness of the hydrography-derived trends at 2000m, but they underestimate the contribution of the temporal sparseness of the hydrography sampling.

There are some basins where both the spatial and temporal mismatch in temperature trend reach high values. This is particularly true in the Southern Ocean, which dominates the spatial distribution of both components (Figure 8d and 8e). In other words, those basins where the largest deep trends, and largest heave-component of the trends, were previously reported (see Figure 2e and Figure 3e) are also those with the largest sampling-related uncertainties. Note that while this comparison focuses on the 2000m depth horizon and may not apply deeper in the water column, we assume the magnitude of the sampling-related uncertainty to decrease with depth as the heave related variability decreases as one moves toward the more quiescent abyssal ocean.

6. Discussion and conclusion

A combination of repeat hydrography and Argo data was used to provide the first assessment of the full-depth global distribution of oceanic temperature changes during the early 21^{st} century. The global ocean has warmed at 2.2 ± 0.2 °C decade^{-1}, which is equivalent to a heat uptake of 0.72 ± 0.09 W m^{-2} and a thermosteric sea-level rise of 0.87 ± 0.13 mm yr^{-1}, in line with previously published values (von Schuckmann et al. 2016; Wijffels et al. 2016). The uptake of heat has a significant vertical structure and our results agree with previous studies in suggesting a combination of mechanisms for storing heat below the upper mixed layer and decreasing the surface warming rate (Meehl et al. 2011; Chen and Tung 2014). The Atlantic and Southern oceans particularly follow that pattern, with negative trends near the surface but significant heat uptake in the remaining part of the water column.

A significant fraction (44%) of the global ocean warming is found in the first seven hundred meters of the water column, half of it being observed in the Indian Ocean. This Indian Ocean's warming, recently attributed to an increased heat transport from the Pacific Ocean via the Indonesian through flow (Lee et al. 2015), is embedded in a large-scale warming pattern encompassing the southern hemisphere extra-tropics, as already noted by Roemmich et al. (2015). This widespread signal extends relatively deep in the water column and still represents a significant fraction of the intermediate warming between 700m and 2000m depth. However, the intermediate layer shows its strongest trends in the North Atlantic Ocean and in the Weddell-Enderby basin in the Atlantic sector of the Southern Ocean that warmed much faster than any other region. This highlights the critical role played by these two regions for the global energy budget, with pronounced vertical overturning cells that connect the surface to the ocean interior and transport the temperature signals to depth in the water column. Finally, repeat hydrography reveals a $\sim$10% contribution of the deep and abyssal layers (below 2000m depth) to the global OHC trend, with a dominant Southern Ocean contribution and an associated warming (0.07 ± 0.06 W m^{-2}) similar to that of the longer 1990's to 2000's trend reported by Purkey and Johnson (2010). This consistent warming rate relative to the previous decade suggests that no accelerated warming was detected in the lower half of the water column during the surface warming slowdown of the 2000's .

A decomposition of the linear trends into a heave (vertical displacements of isopycnal surfaces) and a spiciness (density-compensated changes along isopycnal surfaces) component provides a framework for interpreting the Argo-Hydrography estimates (Bindoff and McDougall 1994). Over the time period considered here, the regional heave and OHC trends are significantly impacted by wind-driven and adiabatic redistribution of water masses, most especially within the upper layer. However, the impact of such redistributions should reduce when globally averaging the full-depth trends, so that the observed global deepening of isopycnals must be predominantly forced by increased heat fluxes from the atmosphere.

The heave/spiciness decomposition reveals that a large fraction of the global ocean heat uptake during the recent decade was associated with a deepening of isopycnal surfaces. This deepening shows large values in the density/depth range of subtropical mode waters, and explains the dominant warming signal found in the southern hemisphere's extratropics. As first hypothesized by Church et al. (1991) and recently confirmed by an analysis of multidecadal upper OHC changes (Häkkinen et al. 2016), this global pattern potentially reflects the lateral spreading of warming signals from high-latitude subduction areas of subtropical mode waters. On the other hand, the spiciness component of the temperature trend is largest within the intermediate layer, and is notably responsible for the warming "hot-spots" observed in the subpolar North Atlantic and in the Southern Ocean that encompass sites of intense vertical mixing associated with mode and intermediate water formation (e.g. Mauritzen et al. 2012).

The present analysis of repeat hydrography data confirms previous results (e.g. Desbruyères et al. 2014) by showing heave-induced temperature changes not only restricted to the upper ocean but reaching down to the deepest portions of the water column. Strong positive values are notably found in the North Atlantic and Southern Ocean, which likely reflects the reduced renewal rates of Labrador Sea Water in the North Atlantic subpolar gyre during the early 2000's (Robson et al. 2014) and Antarctic Bottom Water around Antarctica (Purkey and Jonhson 2012). Those heave-related trends at deep levels are, however, associated with largest uncertainties revealed by the mismatch with the Argo-derived trends at the 2000m interface. Subsampling the full Argo estimates of the trend at 2000m shows that this mismatch results from both the limited number of repeats (temporal mismatch) and the limited number of sections (spatial mismatch) of the hydrography dataset. Both sources of mismatch have their largest contributions in the Southern Ocean, which is where the largest deep trends are observed, and which requires both more reference sections and more frequent occupations. Other regions, such as the Indian and south Atlantic oceans, present smaller mismatches mostly related to temporal sparseness of the hydrography sampling. This indicates that more regular occupations rather than more reference sections would improve the sampling of the decadal changes there. Our analysis further highlights the requirement for the implementation of the systematic observing system *Deep-Argo* that will complement repeat hydrography in capturing the high frequency signals below 2000m depth (Johnson et al. 2015). For the study of long-term (decadal) temperature trends, our results indicate that the Southern Ocean is the priority region deep float deployments.

Overall, the present reconciliation of Argo and repeat hydrography provides a new representation of changes in ocean temperature and heat content from the last decade of sustained observations, while improving uncertainty estimates in the current deep and abyssal observing system. The mechanistic analysis of the temperature change, as applied to the full-depth and global estimates, enabled us to identify regions and layers where the 21^{st} century's warming was either dominantly linked to vertical migration of isopycnal surfaces, or to density-compensated temperature anomalies.

Acknowledgments. This work is a contribution to the DEEP-C project, funded by the British National Environmental Research Council (NERC - grant NE/K004387/1). GO-SHIP CTD data were made available by data originators either as public data on the CCHDO website (http://cchdo.ucsd.edu), where cruise participants can be identified, or directly by cruise PIs. Argo data (http://doi.org/10.17882/42182) were collected and made freely available by the International Argo Program and the national programs that contribute to it (http://www.argo.ucsd.edu, http://argo.jcommops.org). The Argo Program is part of the Global Ocean Observing System. We thank the many investigators who contribute to these observing systems. On behalf of all authors, the corresponding author states that there is no conflict of interest.

References

Bindoff, N. L., and T. J. McDougall, 1994: Diagnosing climate change and ocean ventilation using hydrographic data. *Journal of Physical Oceanography*, **24**, 1137–1152.

Chen, X., and K.-K. Tung, 2014: Varying planetary heat sink led to gobal-warming slowdown and acceleration. *Science*, **345 (6199)**, doi:10.1126/science.1254937.

Church, J. A., J. S. Godfrey, D. R. Jackett, and T. J. McDougall, 1991: A model of sea level rise caused by ocean thermal extension. *Journal of Climate*, **4**, 438–456.

Desbruyères, D., E. L. McDonagh, B. A. King, F. K. Garry, A. T. Blaker, B. I. Moat, and H. Mercier, 2014: Full-depth temperature trends in the norteastern atlantic through the early 21st century. *Geophysical Research Letters*, **41**, doi:10.1002/2014GL061844.

Drijtfhout, S. S., A. T. Blaker, S. A. Josey, A. J. G. Nurser, B. Sinha, and M. A. Balmaseda, 2014: Surface warming hiatus caused by increased heat uptake across multiple ocean basins. *Geophysical Research Letters*, doi:10.1002/2014GL061456.

Durack, P. J., P. J. Gleckler, F. W. Landerer, and K. E. Taylor, 2014: Quantifying underestimates of long-term upper-ocean warming. *Nature climate change*, **4**, 999–1005, doi:10.1038/nclimate2389.

England, M. H., and Coauthors, 2014: Recent intensification of wind-driven circulation in the Pacific and the ongoing warming hiatus. *Nature climate change*, doi:10.1038/nclimate2106.

Ganachaud, A., and C. Wunsch, 2003: Large-Scale Ocean Heat and Freshwater Transport during the World Ocean Circulation Experiment. *Journal of Climate*, **16**, 696–705.

Häkkinen, S., P. B. Rhines, and D. L. Worthen, 2015: Heat content variability in the North Atlantic Ocean in ocean reanalyses. *Geophysical Research Letters*, **42**, doi:10.1002/2015GL063299.

Häkkinen, S., P. B. Rhines, and D. L. Worthen, 2016: Warming of the global ocean: spatial structure and water mass trends. *Journal of Climate*.

Hernàndez-Guerra, A., and L. D. Talley, 2016: Meridional overturning transports at 30s in the indian and pacific oceans in 2002–2003 and 2009. *Progress in Oceanography*, **146**, doi:10.1016/j.pocean.2016.06.005.

Hood, E. M., C. L. Sabine, and B. M. Sloyan, 2010: GO-SHIP Repeat Hydrography Manual: A Collection of Expert Reports and Guidelines. *IOCCP Report Number 14*.

Intergovernmental Panel on Climate Change, C. C. . T. P. S. B., 2013, 2013: *Intergovernmental Panel on Climate Change (IPCC), Climate Change 2013: The Physical Science Basis*. Cambridge Univ. Press, Cambridge, UK.

Johnson, G. C., J. L. Bullister, and N. Gruber, 2005: Labrador Sea Water property variations in the northeastern Atlantic Ocean. *Geophysical Research Letters*, **32**, doi:10.1029/2005GL022404.

Johnson, G. C., J. M. Lyman, and S. G. Purkey, 2015: Informing Deep Argo Array Design Using Argo and Full-Depth Hydrography Section Data. *Journal of Atmospheric and Oceanic Technology*, doi:10.1175/JTECH-D-15-0139.1.

Kostov, Y., K. C. Armour, and J. Marshall, 2014: Impact of the Atlantic meridional overturning circulation on ocean heat storage and transcient climate change. *Geophysical Research Letters*, doi:10.1002/2013GL058998.

Lee, S.-K., W. Park, M. O. Baringer, A. L. Gordon, B. Huber, and Y. Liu, 2015: Pacific origin of the abrupt increase in indian ocean heat content during the warming hiatus. *Nature Geosci.*, doi:10.1038/NGEO2438.

Levitus, S., and Coauthors, 2012: World ocean heat content and thermosteric sea level change (0-2000 m), 1955-2010. *Geophysical Research Letters*, **39**, doi:10.1029/2012GL051106.

Mauritzen, C., A. Melsom, and T. Sutton, 2012: Importance of density-compensated temperature change for deep North Atlantic Ocean heat uptake. *Nature Geosci.*, **5**, doi:10.1038/ngeo1639.

Meehl, G. A., J. M. Arblaster, J. T. Fasullo, A. Hu, and K. E. Trenberth, 2011: Model-based evidence of deep-ocean heat uptake during surface-temperature hiatus periods. *Nature climate change*, **1**, doi:10.1038/NCLIMATE1229.

Palmer, M. D., and Coauthors, 2015: Ocean heat content variability and changes in an esemble of ocean reanalyses. *Climate Dynamics*, doi:10.1007/s00382-015-2801-0.

Purkey, S. G., and G. C. Johnson, 2010: Warming of Global Abyssal and Deep Southern Ocean Waters between the 1990s and 2000s: Contribution to Global Heat and Sea Level Rise Budgets. *Journal of Climate*, **23**, 6336 – 6350, doi:10.1175/2010JCLI3682.1.

Purkey, S. G., and G. C. Jonhson, 2012: Global contraction of Antarctic Bottom Water between the 1980s and 2000s. *Journal of Climate*, **25**, 5830–5844.

Robson, J., D. Hodson, E. Hawkins, and R. Sutton, 2014: Atlantic overturning in decline? *Nature Geosciense*, **7**, doi:10.1038/ngeo2050.

Roemmich, D., J. Church, J. Gilson, D. Monselesan, P. Sutton, and S. Wijffels, 2015: Unabated planetary warming and its ocean structure since 2006. *Nature climate change*, doi:10.1038/NCLIMATE2513.

Roemmich, D., and J. Gilson, 2009: The 2004-2008 mean and annual cycle of temperature, salinity, and steric height in the global ocean from the Argo Program. *Progress in Oceanography*, **82**, 81–100, doi:10.1016/j.pocean.2009.03.004.

Trenberth, K. E., and J. T. Fasullo, 2010: Tracking earth's energy. *Science*, **328**, 316–317.

von Schuckmann, K., and Coauthors, 2016: An imperative to monitor earth's energy imbalance. *Nature climate change*, doi:10.1038/NCLIMATE2876.

Wijffels, S., D. Roemmich, D. Monselesan, J. Church, and J. Gilson, 2016: Ocean temperatures chronicle the ongoing warming of earth. *Nature climate change*, **6**, 116–118, doi: 10.1038/nclimate2924.

LIST OF FIGURES

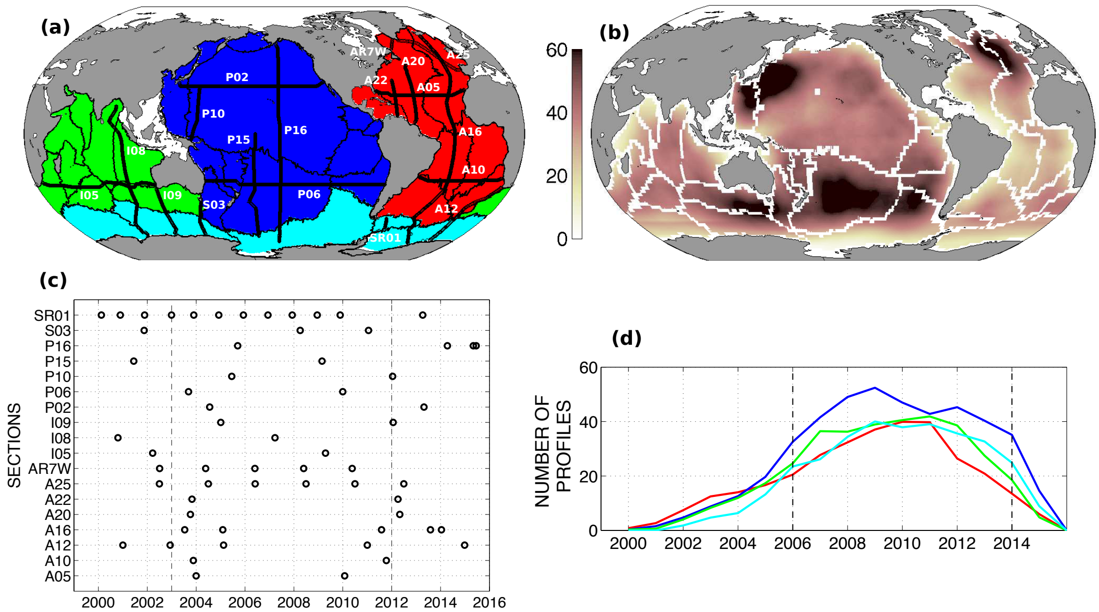

FIG. 1. Spatial and temporal distribution of the Argo and repeat hydrography datasets. (a) The locations of the 18 hydrographic lines and the bathymetry-defined basins grouped into Atlantic (red), Pacific (blue), Indian (green) and Southern (light blue) oceans. (b) The yearly-average number of Argo profiles used within 2°x2° grid boxes between January 2006 and December 2014. (c) The temporal periods covered by the individual hydrography datasets (circles indicate the time of each section occupation). The dashed lines indicate the average time span covered by the repeat hydrography dataset, obtained by averaging the dates of the first and last repeats of all sections. (d) The yearly time series of the number of Delayed-Mode Argo profiles used within 2°x2° grid boxes for each of the four main oceans (same colour code as (a)). The dashed lines indicate the period considered for the Argo analysis (January 2006 - December 2014).

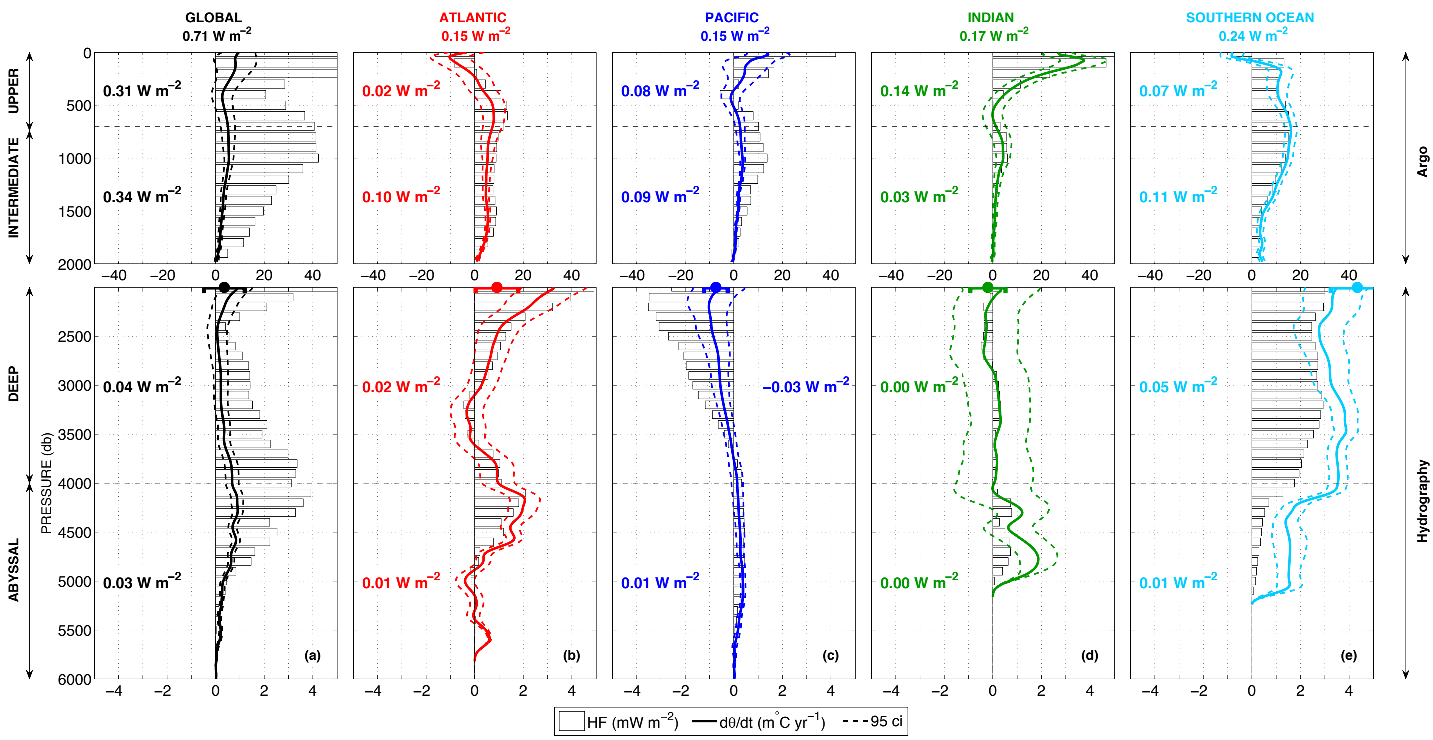

FIG. 2. The surface-to-bottom profiles of temperature trend (solid lines) for the (a) global, (b) Atlantic, (c) Pacific, (d) Indian and (e) Southern Ocean. The associated 95% confidence intervals are shown in dashed lines. The bars indicate the contribution of 100m-thick layers to the global heat uptake (relative to global surface area). Numerical values between horizontal dashed lines indicate the OHU within the upper (0-700m), intermediate (700m-2000m), deep (2000m-4000m) and abyssal (4000m-6000m) layers. Note the different x-axis scales used for Argo and hydrography-related profiles. Dots indicate the Argo-derived trend values and uncertainties at 2000m depth.

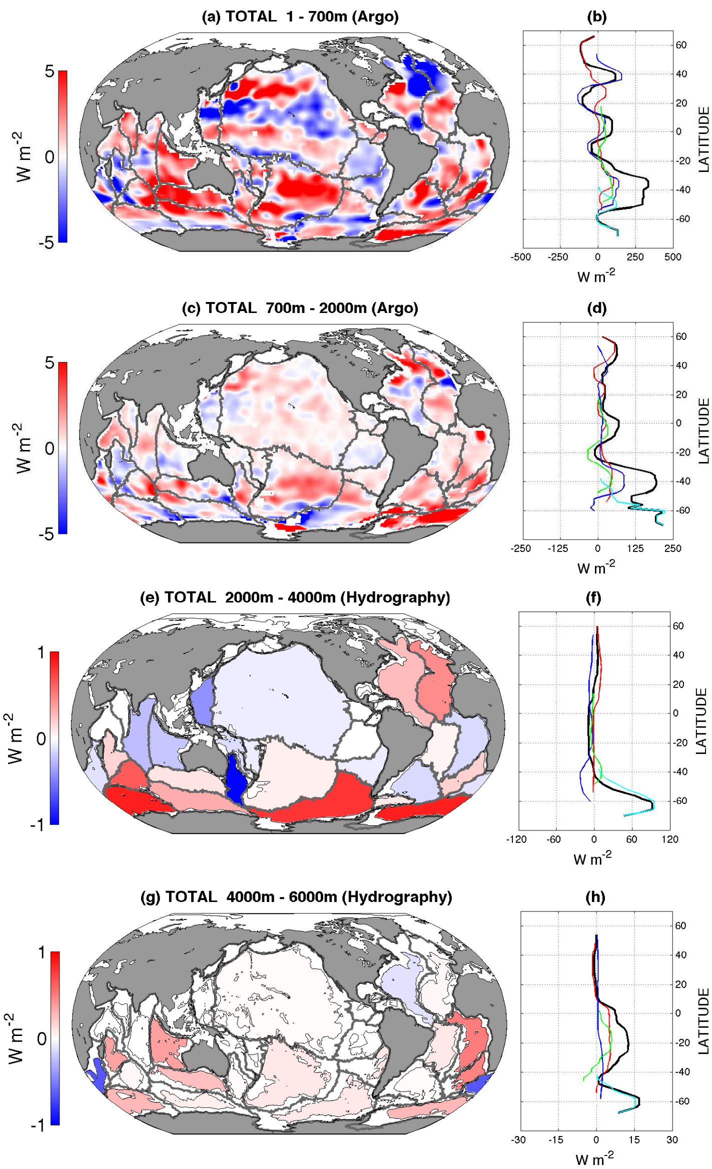

FIG. 3. The spatial distribution of local heat content trend within (a) the upper 0-700m layer, (b) the intermediate 700m-2000m layer, (c) the deep 2000m-4000m layer and (d) the abyssal 4000m-6000m layer. Argo values are contoured depth-average of a 2° grid. Repeat hydrography analysis gives single values for each basin. Thin black line in (e) and (g) indicate the 2000m and 4000m isobaths, respectively. Note the different colour scales used for Argo and hydrography-related values. The right panels show the zonally-averaged profiles for each layer and the related contributions of the Atlantic (red), Pacific (blue), Indian (green) and Southern (light blue). Units are W m^{-2}.

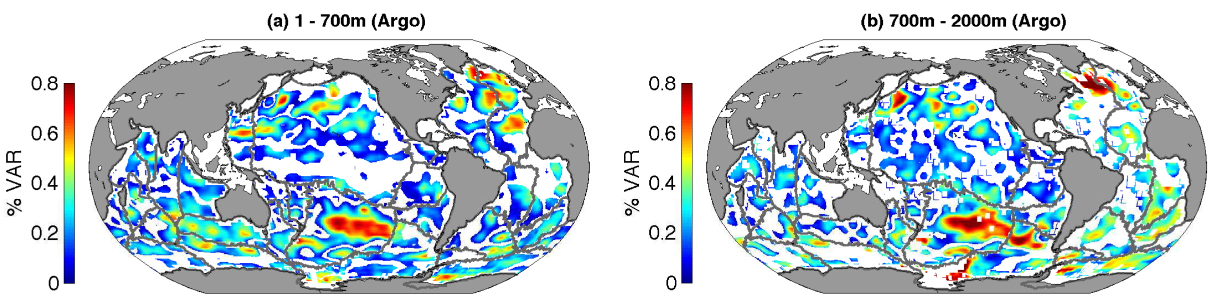

FIG. 4. The percentage of variance explained by the linear temperature trend for (a) the upper layer and (b) the intermediate layer. Regions where the linear temperature trends falls within the 95% confidence interval are masked in white (see equation 1 and text for details).

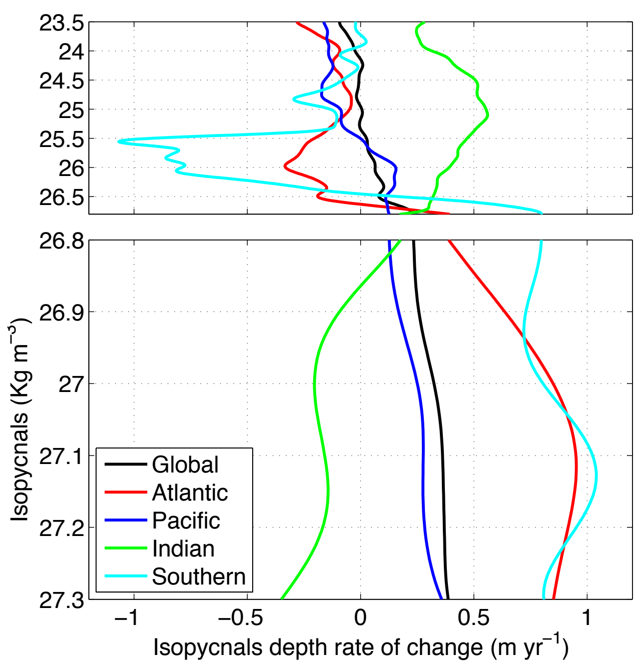

FIG. 5. The rate of change of the depth of isopycnal surfaces for the global (black), Atlantic (red), Pacific (blue), Indian (green) and Southern Ocean (light blue). Positive values mean that isopycnal are increasing their depth. Units are m yr^{-1}.

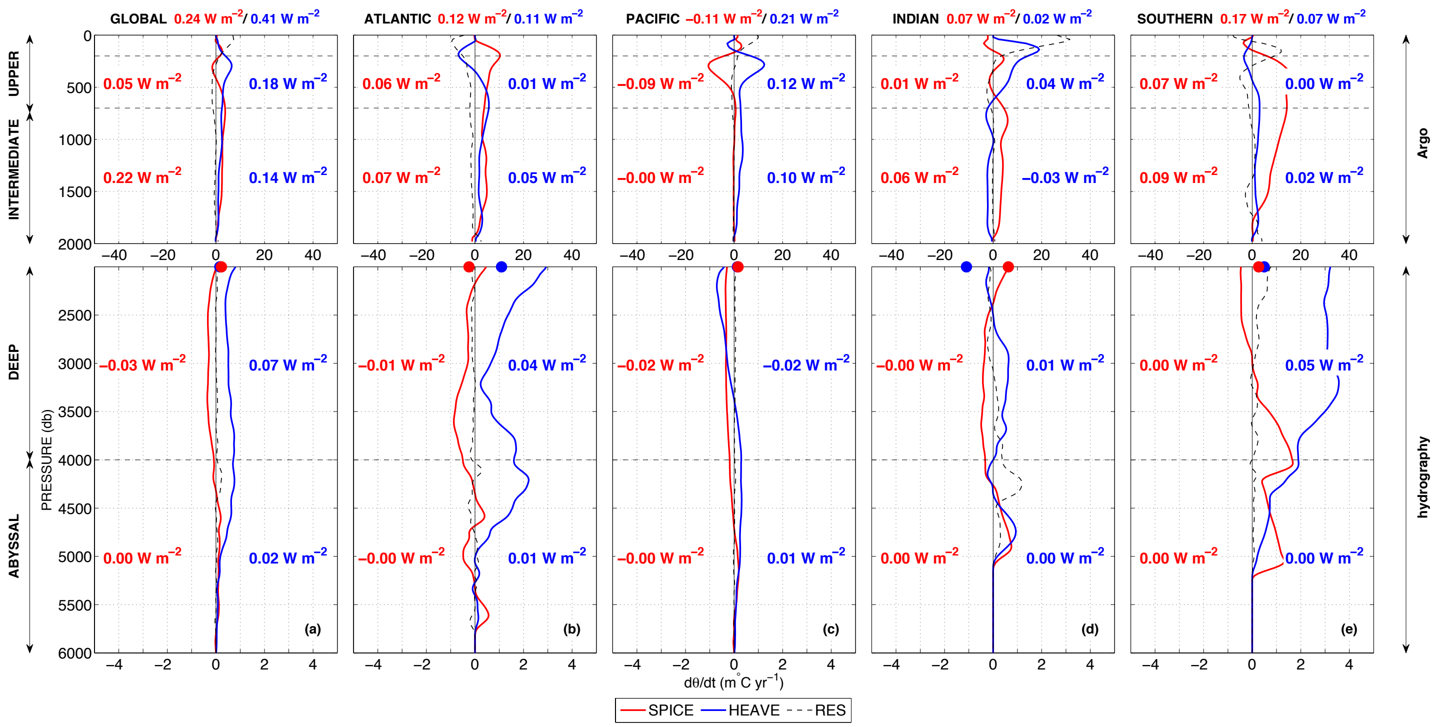

FIG. 6. The surface-to-bottom profiles of temperature trend decomposed into a heave (blue) and a spiciness change (red) components for the (a) global, (b) Atlantic, (c) Pacific, (d) Indian and (e) Southern Ocean. The dashed lines indicate the residual term of the decomposition. Numerical values indicate the OHU within the upper (0-700m), intermediate (700m-2000m), deep (2000m-4000m) and abyssal (4000m-6000m) layers associated with heave (blue) and spiciness changes (red). Note the different x-axis scales used for Argo and hydrography-related profiles. Dots indicate the Argo-derived trend values and uncertainties at 2000m depth for both components.

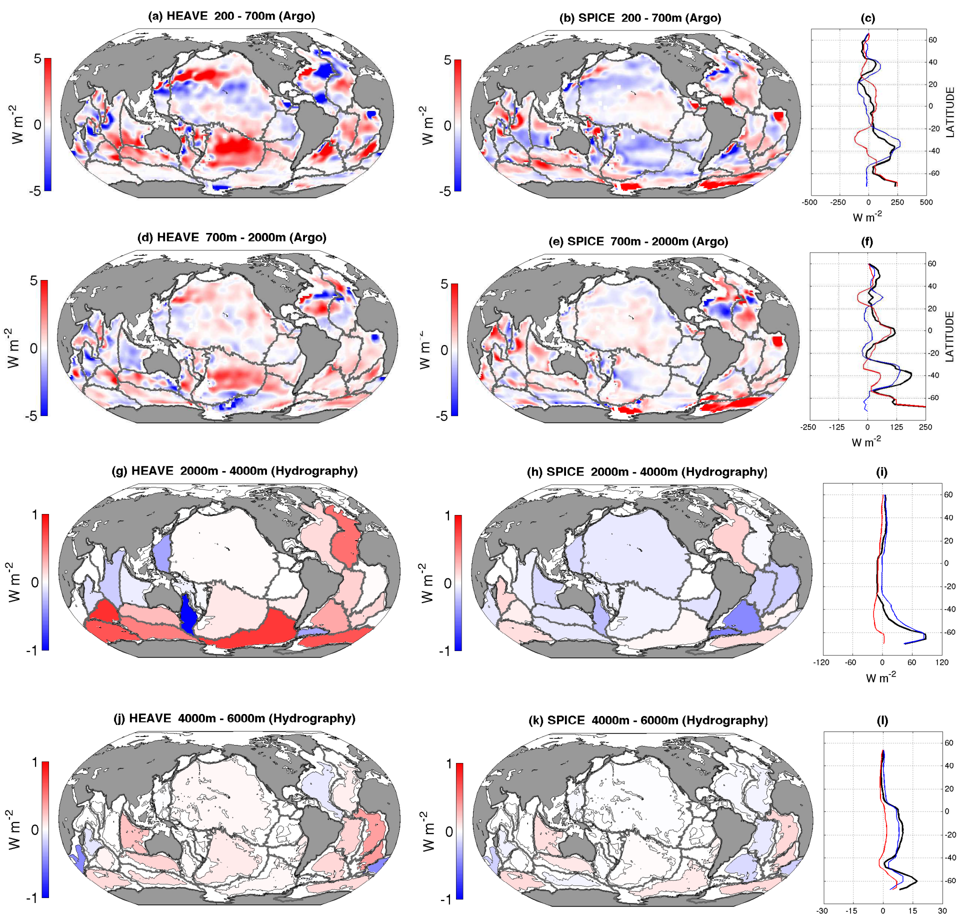

FIG. 7. The spatial distribution of local heat content trend associated with the heave component within (a) the upper 100-700m layer, (d) the intermediate 700m-2000m layer, (g) the deep 2000m-4000m layer and (j) the abyssal 4000m-6000m layer. Similarly, the spice component is shown in (b), (e), (h) and (k), and the zonally-averaged distributions of heave (blue) and spiciness changes (red) are shown in (c), (f), (i) and (l). Note the different colour scales used for Argo and hydrography-related values. Thin black line in (g,h) and (j,k) indicate the 2000m and 4000m isobaths, respectively. Units are W m^{-2}.

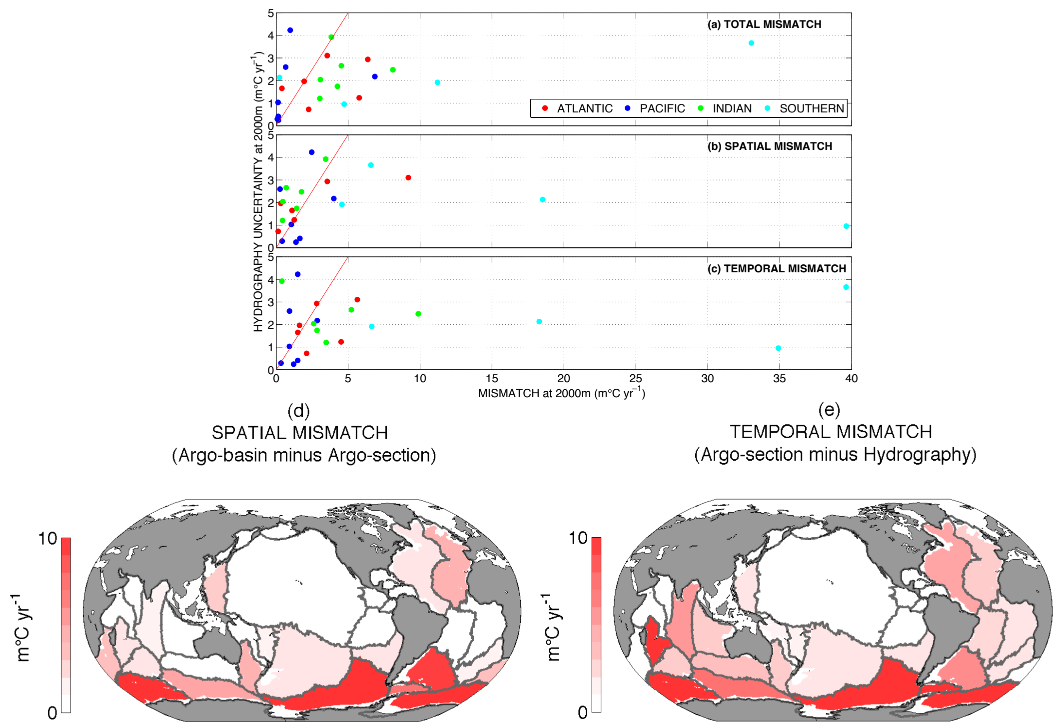

FIG. 8. (a) The comparison of the hydrography-derived uncertainty (see Section 2b) with (a) the sampling-related mismatch (computed as the absolute difference between the hydrography-derived trends at 2000m and the full Argo-derived trends at 2000m), (b) the spatial component of the sampling-related mismatch (computed as the absolute difference between the full Argo-derived trends at 2000m and the Argo-derived trends at 2000m subsampled along the hydrography cruise tracks), (c) the temporal component of the sampling-related mismatch (computed as the absolute difference between the hydrography-derived trends at 2000m and the Argo-derived trends at 2000m subsampled along the hydrography cruise tracks). Colours indicate whether a basin belongs to the Atlantic (red), Pacific (blue), Indian (green) or Southern (cyan) oceans. (d,e) The spatial distribution of the spatial and temporal component of the sampling-related mismatch, respectively.